Research Article Vol. 5, No. 4 / April 2018 / Optica 495

Dichroism-sensitive photoacoustic computed tomography

Yuan Qu,[1,†] Lei Li,[2,†] Yuecheng Shen,[2] Xiaoming Wei,[2] Terence T. W. Wong,[1,2] Peng Hu,[1] Junjie Yao,[1,3] Konstantin Maslov,[2] and Lihong V. Wang[2,*]

[1]Department of Biomedical Engineering, Washington University in St. Louis, St. Louis, Missouri 63130, USA
[2]Caltech Optical Imaging Laboratory, Andrew and Peggy Cherng Department of Medical Engineering and Department of Electrical Engineering, California Institute of Technology, Pasadena, California 91125, USA
[3]Current address: Photoacoustic Imaging Laboratory, Department of Biomedical Engineering, Duke University, Durham, North Carolina 27708, USA
*Corresponding author: LVW@caltech.edu

Received 16 March 2018; accepted 28 March 2018 (Doc. ID 325859); published 18 April 2018

Photoacoustic computed tomography (PACT), a fast-developing modality for deep tissue imaging, images the spatial distribution of optical absorption. PACT usually treats the absorption coefficient as a scalar. However, the absorption coefficients of many biological tissues exhibit an anisotropic property, known as dichroism or diattenuation, which depends on molecular conformation and structural alignment. Here, we present a novel imaging method called dichroism-sensitive PACT (DS-PACT), which measures both the amplitude of tissue's dichroism and the orientation of the optic axis of uniaxial dichroic tissue. By modulating the polarization of linearly polarized light and measuring the alternating signals through lock-in detection, DS-PACT can boost dichroic signals from biological tissues. To validate the proposed approach, we experimentally demonstrated the performance of DS-PACT by imaging plastic polarizers and *ex vivo* bovine tendons deep inside scattering media. We successfully detected the orientation of the optic axis of uniaxial dichroic materials, even at a depth of 4.5 transport mean free paths. We anticipate that the proposed method will extend the capability of PACT to imaging tissue absorption anisotropy.

OCIS codes: (170.3880) Medical and biological imaging; (170.5120) Photoacoustic imaging; (100.1930) Dichroism; (290.5855) Scattering, polarization.

https://doi.org/10.1364/OPTICA.5.000495

1. INTRODUCTION

Medical imaging using non-ionizing radiation can discover and monitor diseases without hazard to the human body [1,2]. Photoacoustic (PA) tomography (PAT) combines non-ionizing photons and low-scattering ultrasound to achieve high optical contrast and high spatial resolution imaging at depths beyond the optical diffusion limit, given by the transport mean free path (l_t') [3–5]. Nevertheless, conventional PAT commonly treats the absorption coefficient as a scalar variable, which does not take the absorption anisotropy of biological tissue into consideration. In practice, however, many biological tissues exhibit dichroism, which means photons in different polarization states traveling through the tissue experience different degrees of absorption. Dichroism, also known as diattenuation, is related to molecular conformation and structural alignment. For example, amyloid, a hallmark of a wide spectrum of protein aggregation disorders, is dichroic [6]. Because PAT converts a small fractional change in the optical absorption coefficient to an equal fractional change in the PA signal, the ratio of the latter to the former, defined as the relative sensitivity to optical absorption, is 100% [7]. Thus, it could be an ideal modality to study the dichroism of biological tissues. Very recently, PA microscopy with optical resolution has demonstrated its capability to image dichroism [6]. However, the demonstrated depth is within the ballistic regime, which is too shallow for many preclinical and clinical applications.

PA computed tomography (PACT) is an embodiment of PAT that provides up to multiple centimeters' imaging depth in tissues with high spatial resolution [8–11]. Here, we present a new approach, called dichroism-sensitive PACT (DS-PACT), which we developed by upgrading a conventional PACT system [12] for dichroism measurement. Benefiting from the deep penetration of PACT, the new approach can image the dichroism of biological tissue at depths beyond the transport mean free path. Moreover, by modulating the polarization of linearly polarized light and measuring the alternating signals through lock-in detection [13], DS-PACT can significantly enhance the imaging contrast among biological tissues with different dichroism, and can also image the orientation of the optic axis of uniaxial dichroic tissue. We first investigated the principle of our approach, then we demonstrated it by imaging the dichroism of both plastic polarizers and biological tissues (bovine tendon) buried deep inside scattering media.

2. METHODS

A. Experimental Setup

The PACT system used in this study (Fig. 1) was upgraded from that in our previous work [12]. A frequency-doubled Nd:YAG laser (LS-2137, LOTIS) at 532 nm with a 10 Hz pulse repetition rate was used for excitation. The output laser beam was vertically polarized. A half-wave plate was used to rotate the polarization of the linearly polarized laser beam. A stepper motor triggered by a function generator rotated the half-wave plate so that the polarization angle of the excitation light before entering the scattering medium was rotated with a period of 32.00 s (corresponding to a rotation frequency $f_M = 0.03125$ Hz). A concave lens then expanded the incident light to a diameter of ~2.5 cm on the sample surface. The maximum light fluence on the surface of our sample was ~15 mJ/cm^2, within the American National Standards Institute safe exposure limit [14].

While illuminating the sample with polarization-rotated light, we collected a sequence of conventional PACT images. The PA signals were detected by a full-ring ultrasonic transducer array with a 5 cm diameter (Imasonic, 5 MHz central frequency, more than 80% one-way bandwidth, and 512 elements). Each element (10 mm high, 0.3 mm pitch, and 0.1 mm inter-element space) was arc-shaped to produce an axial focal distance of 19.8 mm in the imaging plane. The imaging region at the center of the full-ring transducer array consisted of the foci of all 512 elements, and was approximately 20 mm in diameter and 1 mm in thickness. The in-plane resolution was quantified as ~100 μm [12]. The data acquisition system had 64 channels, with eight-fold multiplexing. The cross-sectional imaging speed was 1.6 s per frame. To address the acoustic inhomogeneity between the dichroic materials (DMs) and medium, the half-time image reconstruction was applied in combination with the universal back-projection reconstruction algorithm [15].

Unless otherwise stated, the DMs were embedded in agar gels (3% agar in distilled water). To introduce scattering, on top of the gel, we stacked an additional layer of a scattering medium (0.25% Intralipid and 3% agar in distilled water, with a reduced scattering coefficient of ~0.25 mm^{-1} and a transport mean free path l_t' of ~4 mm). By varying the thicknesses of the scattering layer from 0 mm (no scattering medium) to 20 mm, we quantified the system performance at different depths.

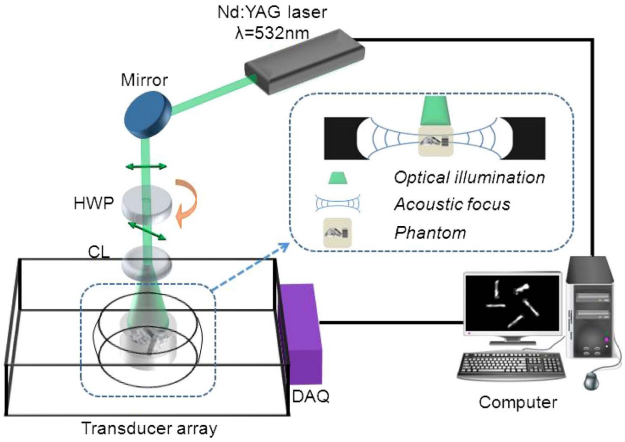

Fig. 1. Experimental setup of DS-PACT. The polarization of linearly polarized light is modulated by a half-wave plate, which is driven by a stepper motor. The light is then expanded by a concave lens. HWP, half-wave plate; CL, concave lens; DAQ, data acquisition system.

B. Operating Principle

Here, we describe the operating principle of DS-PACT. When the excitation light has a polarization angle ϕ, the PA amplitude $\mathrm{PA}(\vec{r},\phi)$ defined in the imaging plane is a function of both the spatial position $\vec{r}$ and the polarization angle ϕ. Mathematically, $\mathrm{PA}(\vec{r},\phi)$ can be represented as the product of the optical absorption coefficient $\mu_a(\vec{r},\phi)$ of the biological tissue and the local light fluence $F(\vec{r},\phi)$ [16]:

$$\mathrm{PA}(\vec{r},\phi) \propto \mu_a(\vec{r},\phi)F(\vec{r},\phi). \tag{1}$$

In our study, the DMs are assumed to be uniaxial. Thus, the absorption coefficient $\mu_a(\vec{r},\phi)$ in Eq. (1) along the polarization direction is [17]

$$\mu_a(\vec{r},\phi) = \mu_{a,o}(\vec{r})\frac{n^3(\vec{r},\phi)}{n_o^3(\vec{r})}\cos^2(\phi-\theta(\vec{r})) + \mu_{a,e}(\vec{r})\frac{n^3(\vec{r},\phi)}{n_e^3(\vec{r})}\sin^2(\phi-\theta(\vec{r})). \tag{2}$$

Here, $\theta(\vec{r})$ is the orientation of the optic axis of the biological tissue at the position $\vec{r}$. $n(\vec{r},\phi)$, $n_o(\vec{r})$, and $n_e(\vec{r})$, accounting for the refraction, are, respectively, the spatial distributions of the real part of the refractive index along the polarization direction, the direction perpendicular to the optic axis, and the direction parallel to the optic axis. $\mu_{a,o}(\vec{r})$ and $\mu_{a,e}(\vec{r})$ are the spatial distributions of the absorption coefficient perpendicular and parallel to the optic axis, respectively. The subscripts o and e stand for the words "ordinary" and "extraordinary." For many anisotropic tissues, such as tendon, the fractional change of the refractive index $\Delta n/\bar{n} = (n_o - n_e)/(\frac{n_o+n_e}{2})$ is on the order of 10^{-4} [18]. Therefore, we assume here that $n(\vec{r},\phi) \approx n_e(\vec{r}) \approx n_o(\vec{r})$ and reduce Eq. (2) as follows:

$$\begin{aligned}\mu_a(\vec{r},\phi) &\approx \mu_{a,o}(\vec{r})\cos^2(\phi-\theta(\vec{r})) + \mu_{a,e}(\vec{r})\sin^2(\phi-\theta(\vec{r})),\\ &= \frac{\mu_{a,o}(\vec{r})+\mu_{a,e}(\vec{r})}{2} + \frac{\mu_{a,o}(\vec{r})-\mu_{a,e}(\vec{r})}{2}\cos 2(\phi-\theta(\vec{r})),\\ &= \bar{\mu}_a(\vec{r})\left[1+\frac{\Delta\mu_a(\vec{r})}{2\bar{\mu}_a(\vec{r})}\cos 2(\phi-\theta(\vec{r}))\right],\end{aligned} \tag{3}$$

where $\Delta\mu_a = \mu_{a,o}(\vec{r}) - \mu_{a,e}(\vec{r})$ and $\bar{\mu}_a(\vec{r}) = \frac{\mu_{a,o}(\vec{r})+\mu_{a,e}(\vec{r})}{2}$, respectively, are the variation and the average of the absorption coefficient. For tendon, $\Delta\mu_a(\vec{r})/2\bar{\mu}_a(\vec{r})$ can be as high as 0.2 [18], and thus induces easily detectable changes in the PA amplitude.

Because the fractional change of the refractive index is on the order of 10^{-4}, we approximate $F(\vec{r},\phi)$ to $F(\vec{r})$. Providing that ϕ is rotated with a frequency of f_M, Eq. (1) can be rewritten as

$$\mathrm{PA}(\vec{r},t) \propto \bar{\mu}_a(\vec{r})F(\vec{r})\left[1+\frac{\Delta\mu_a(\vec{r})}{2\bar{\mu}_a(\vec{r})}\cos 2(2\pi f_M t-\theta(\vec{r}))\right]. \tag{4}$$

As we can see from Eq. (4), the PA amplitude oscillates at a frequency of $2f_M$. Here, we notice that the initial phase, $2\theta(\vec{r})$, is twice the orientation angle of the optic axis.

Figure 2 is a schematic of the image reconstruction process of DS-PACT. First, as shown in Fig. 2(a), a sequence of conventional PACT images is acquired at a frame rate of 0.625 Hz. The polarization of the incident light is rotated at 11.25°/s. Figure 2(b) then plots the PA amplitude at one representative spatial position along the time sequence. As shown in Fig. 2(b), the PA amplitude oscillates with a period of 16 s, which corresponds to the frequency of $2f_M = 0.0625$ Hz from Eq. (4). The Fourier transform of the time sequence in Fig. 2(b) is shown in amplitude in Fig. 2(c). The direct current term at zero frequency corresponds to $\bar{\mu}_a(\vec{r})F(\vec{r})$ in Eq. (4), while the peak located at the frequency of 0.0625 Hz corresponds to the alternating current term in Eq. (4), and we will lock in to this term. By calculating the Fourier transform of the PA amplitude from the sequence of reconstructed conventional PACT images [Fig. 2(a)] pixel by pixel (over the entire field of view), we can obtain images representing the amplitude of dichroism and the initial orientation angle of the optic axis. A reconstructed image based on the amplitude of dichroism is shown in Fig. 2(d). The reconstructed image that denotes the orientation angle $\theta(\vec{r})$ of the optic axis of the DM is shown in Fig. 2(e). To highlight the DMs in Fig. 2(e), the orientation information is shown only at positions where the corresponding PA amplitudes are above a certain threshold value. In our work, the threshold was set at four times the noise level in the conventional PACT images, where the noise level was estimated as the standard deviation of the background signal outside the object region. We also emphasize here that DS-PACT has the potential to detect dichroism deep inside scattering media. The lock-in detection strategy can theoretically scale the signal-to-noise ratio (SNR) with the number of frames N as $\sqrt{N}$ [19], so that we can detect a weak response to polarization below a thick scattering medium by increasing N.

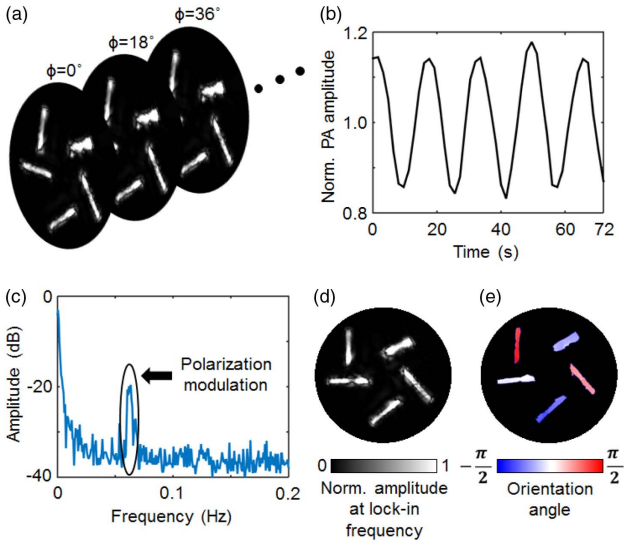

Fig. 2. Schematic of image reconstruction. (a) A sequence of conventional PACT images is acquired at a frame rate of 0.625 Hz, rotating the polarization of the incident light at 11.25°/s. (b) Normalized PA amplitude as a function of time at one representative spatial point. PA(t) is normalized with respect to its average. (c) Fourier spectrum of PA(t). The peak located at 0.0625 Hz corresponds to the alternating PA signals due to the modulated polarization. (d) DS-PACT image reconstructed by the amplitude of the lock-in term in Eq. (4). (e) Color-coded orientation angle map of the sample, which is reconstructed from the phase of the lock-in term in Eq. (4).

3. RESULTS

Having demonstrated the operating principle, we now quantify the performance of DS-PACT by imaging the dichroism of linear polarizers. The sample was made by embedding two plastic linear polarizers and two pieces of silicone rubber in the agar medium [Fig. 3(a)]. Then 900 conventional PACT images spanning 90 modulation cycles were collected. In the reconstructed conventional PACT image [Fig. 3(b)], both the linear polarizers and silicone rubber can be visualized. The PA amplitude ratio of the linear polarizers to the silicone rubber was approximately equal to −12.04 dB [Fig. 3(c)]. Although the silicone rubber has a PA amplitude that is four times the value of the linear polarizer, the PA amplitude of the silicone rubber did not vary with the modulated polarization of the excitation light (Visualization 1). In contrast, the PA amplitudes of the linear polarizers were modulated by the polarization of the excitation light. Figure 3(d) shows the PA amplitudes of these four objects. As we can see from the figure, the PA amplitudes of the two linear polarizers have a π phase shift, because their optic axes are mutually perpendicular. The reconstructed DS-PACT images are shown in Figs. 3(e) and 3(f). Figure 3(e) is the DS-PACT image, reconstructed by the amplitude of the lock-in term in Eq. (4) and highlighting the spatial distribution of the linear polarizers. In this image, the silicone rubber is much less prominent than the linear polarizers because their PA amplitudes are not modulated by the polarization. The temporal-frequency amplitude ratio at $2f_M$ of the linear polarizers to the silicone rubber was approximately 17.58 dB [Fig. 3(c)]. Figure 3(f) is a color-coded orientation angle map of the linear polarizers, reconstructed from the phase of the lock-in term in Eq. (4). Therefore, unlike conventional PACT, DS-PACT can highlight the materials with dichroism and detect the orientations of their optic axes, while suppressing the materials without dichroism. These results are consistent with our hypotheses, supporting the operating principle.

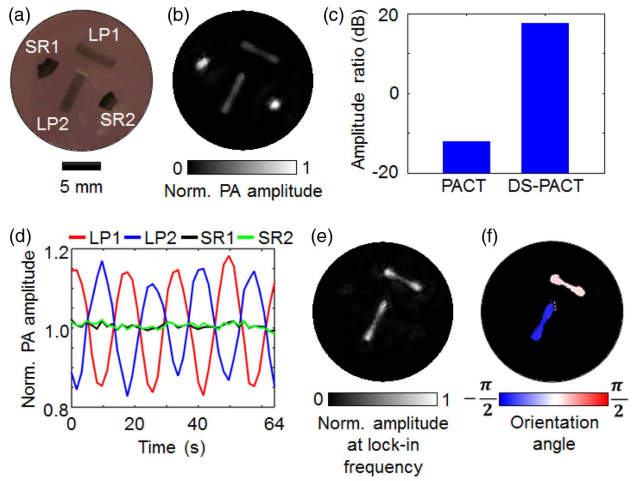

Fig. 3. DS-PACT of linear polarizers and silicone rubber. (a) Photograph of the sample without any scattering medium. LP, linear polarizer; SR, silicone rubber. (b) Conventional PACT image averaged over 900 frames. (c) Amplitude ratio of the linear polarizers to the silicone rubber in the conventional PACT image and in the DS-PACT image. (d) Normalized PA amplitudes of the linear polarizers and silicone rubber. (e) DS-PACT image reconstructed by the amplitude of the lock-in term in Eq. (4). (f) Orientation angle map of the linear polarizers, in which two pieces of silicone rubber are not shown.

Light gradually loses its original polarization when propagating deeper and deeper in a scattering medium. As a result, the amplitude of the lock-in term gradually decreases and is finally overwhelmed by noise. Therefore, to investigate the performance of DS-PACT at different depths in scattering media, we embedded five linear polarizers at different orientations in the agar medium [Fig. 4(a)] and varied the thickness of the scattering layer above. We analyzed the modulation depth $\Delta\mathrm{PA}(D)$ as a function of the thickness D of the scattering medium. Here, $\Delta\mathrm{PA}(D)$ is defined as the difference between the maximum PA amplitude and the minimum PA amplitude divided by the average PA amplitude in a single modulation cycle. The results of $\Delta\mathrm{PA}(D)$, obtained by averaging over 90 modulation cycles, are normalized by the largest value. As shown in Fig. 4(b), $\Delta\mathrm{PA}(D)$ decays exponentially with increasing thickness D, until it reaches $D = 18$ mm. The data were fitted with a decay constant of 0.12 mm^{-1}, which describes the speed of depolarization. This result indicates that DS-PACT can still function at a depth of 18 mm, because the local excitation is still partially polarized. When the thickness reaches $D = 20$ mm, $\Delta\mathrm{PA}(D)$ is dominated by noise, which indicates the depth limit in our current experimental condition. For three representative scattering media with thicknesses of $D = 2$ mm, 18 mm, and 20 mm, Fig. 4(c) shows the reconstructed images using conventional PACT, and all the linear polarizers are visible in all three images. We also reconstructed the images using DS-PACT. The amplitude image and the orientation angle map are shown in Figs. 4(d) and 4(e). As we can see from the figure, even below an 18 mm thick scattering medium, the linear polarizers are still visible, and the orientations of their optic axes can still be detected. However, when $D = 20$ mm, the amplitude of the lock-in term becomes too weak, so that the linear polarizers disappear from the DS-PACT image [Fig. 4(d)], and the orientation angle map is no longer correct [Fig. 4(e)]. Therefore, we conclude that under our current experimental conditions DS-PACT can image linear polarizers at 18 mm deep, which is approximately equal to 4.5 l_t'.

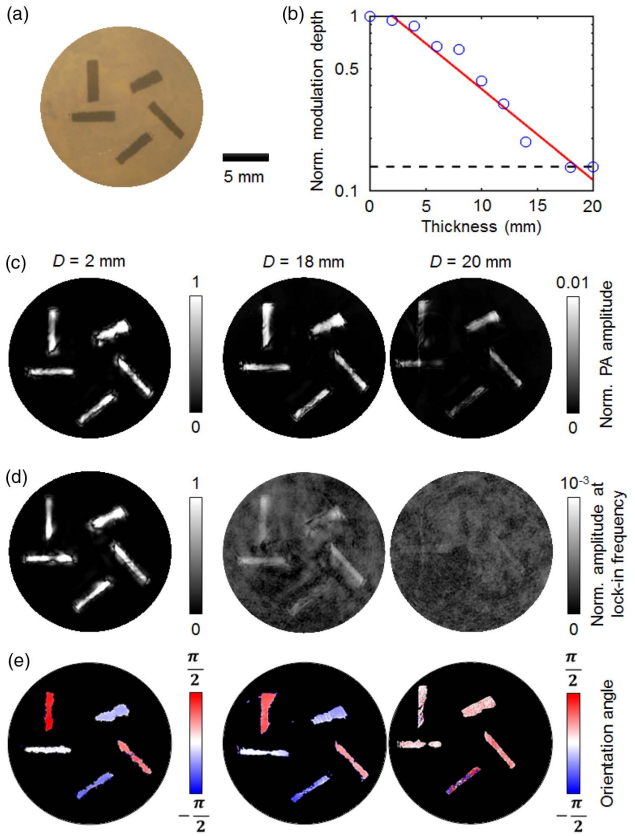

Fig. 4. DS-PACT of the linear polarizers. (a) Photograph of the sample without any scattering medium. The sample contains five linear polarizers placed at different orientations. (b) Modulation depth of the PA amplitude acquired as a function of thickness D of the scattering medium, up to 20 mm. The red solid line indicates the exponential fit to the measured data. The black dashed line represents the noise level. (c) Conventional PACT images. (d) Amplitude images using DS-PACT. (e) Orientation angle maps of the linear polarizers. Supplement 1 shows images at more depths.

To show that DS-PACT is suitable for biological applications, we also formed images of biological tissue in scattering media. In experiments, we imaged two pieces of *ex vivo* bovine tendon [18] [Fig. 5(a)], a typical dichroic tissue, at various depths below the scattering medium. Bovine tendon has a high concentration of collagen, which exhibits optical diattenuation and absorbs strongly at 532 nm. Figure 5(b) shows the normalized modulation depth $\Delta\mathrm{PA}(D)$ for the bovine tendon as a function of D, with a result similar to that in Fig. 4(b). $\Delta\mathrm{PA}(D)$ decays exponentially until it reaches $D = 13$ mm, and finally encounters the noise level at $D = 15$ mm. The decay constant of the best-fitting line was 0.1 mm^{-1}. For three representative scattering media with thicknesses of $D = 2$ mm, 13 mm, and 15 mm, Fig. 5(c) shows the reconstructed images using conventional PACT, and both pieces of bovine tendon are visible in all three images. We also reconstructed the images using DS-PACT. The amplitude images and the orientation angle maps are shown in Fig. 5(d) and 5(e), respectively. As we can see from the figure, the bovine tendons are still visible when the scattering medium has a thickness of $D = 13$ mm, and the orientation of their optic axes can still be detected. However, when $D = 15$ mm, the amplitude of the lock-in term becomes too weak, so that the two pieces of bovine tendon disappear from the DS-PACT image [Fig. 5(d)], and the orientation angle map is no longer correct [Fig. 5(e)]. Thus, the deepest penetration of DS-PACT demonstrated using the bovine tendon in our experiments was 13 mm, approximately equal to 3.25 l_t'.

4. DISCUSSION AND CONCLUSIONS

Given a DM that shows varying absorption as a function of the polarization angle, the fluence in the region underneath the DM will show a similar variation. As a result, a non-dichroic absorber located in this region will also exhibit a modulation in the PA amplitude as a function of the polarization angle. Nevertheless, a non-dichroic absorber still can be differentiated from a dichroic absorber.

For a non-dichroic absorber located below a dichroic absorber, its PA amplitude can be expressed as

$$[\mathrm{PA}(\vec{r},\phi)]_{\mathrm{ND}} \propto [\mu_a(\vec{r})]_{\mathrm{ND}} F(\vec{r},\phi), \tag{5}$$

where $[\mu_a(\vec{r})]_{\mathrm{ND}}$ is the absorption coefficient of the non-dichroic absorber, which is independent of the polarization of the excitation light. The local fluence $F(\vec{r},\phi)$ can be expressed as

$$F(\vec{r},\phi) = \overline{F}(\vec{r})[1 - \alpha \cos 2(2\pi f_M t - \theta(\vec{r}\,'))], \tag{6}$$

where $0 < \alpha < 1$, $\phi = 2\pi f_M t$, $\theta(\vec{r}\,')$ is the orientation angle of the top dichroic absorber at $\vec{r}\,'$, and $\overline{F}(\vec{r})$ is the average of local

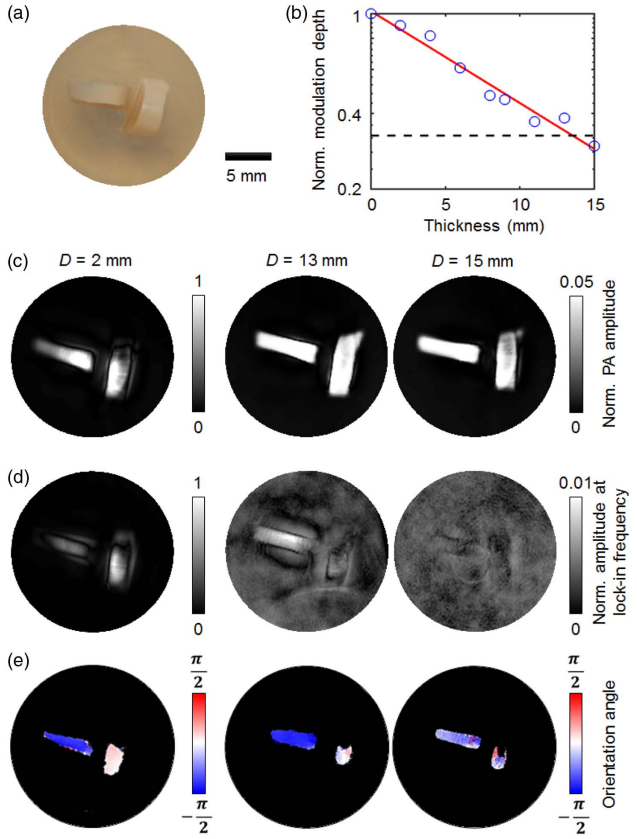

Fig. 5. DS-PACT of bovine tendons. (a) Photograph of the sample without any scattering medium. The sample contains two pieces of bovine tendon, which are placed perpendicular to each other. (b) Modulation depth of the PA amplitude acquired with increasing thickness D of the scattering medium, up to 15 mm. The red solid line indicates the exponential fit to the measured data. The black dashed line represents the noise level. (c) Conventional PACT images. (d) Amplitude images using DS-PACT. (e) Orientation angle maps of the two pieces of bovine tendon.

light fluence. It is clear that $F(\vec{r},\phi)$ contains an oscillatory term due to the fluence modulation induced by the dichroic absorber above, so that the measured PA amplitude $[\mathrm{PA}(\vec{r},\phi)]_{\mathrm{ND}}$ has a modulation frequency, $2f_M$. Moreover, this modulation should have a π phase shift from the modulation of the dichroic absorber, because the more photons the top dichroic absorber absorbed, the fewer photons the non-dichroic absorber could absorb. As a result, a false orientation angle calculated by our method, shown by the non-dichroic absorber, is perpendicular to the orientation angle of the top dichroic absorber.

Similarly, for another dichroic absorber located at the same depth, the PA amplitude can be expressed as

$$
\begin{aligned}
[\mathrm{PA}(\vec{r},\phi)]_D &\propto [\mu_a(\vec{r},\phi)]_D F(\vec{r},\phi) \\
&\approx \overline{\mu}_a(\vec{r})\overline{F}(\vec{r})\left[1+\frac{\Delta\mu_a(\vec{r})}{2\overline{\mu}_a(\vec{r})}\cos 2(2\pi f_M t-\theta(\vec{r}))\right] \\
&\quad -\overline{\mu}_a(\vec{r})\overline{F}(\vec{r})\alpha\cos 2(2\pi f_M t-\theta(\vec{r}\,')) \\
&\quad -\frac{\overline{F}(\vec{r})\Delta\mu_a(\vec{r})\alpha}{2}\cos 2(2\pi f_M t-\theta(\vec{r})) \\
&\quad \times\cos 2(2\pi f_M t-\theta(\vec{r}\,')). \qquad (7)
\end{aligned}
$$

Since both the absorption coefficient $[\mu_a(\vec{r},\phi)]_D$ and the local fluence $F(\vec{r},\phi)$ contain the oscillatory term, their product $[\mathrm{PA}(\vec{r},\phi)]_D$ has a second-harmonic term at $4f_M$ in addition to the fundamental modulation frequency of $2f_M$. Therefore, we should be able to distinguish the non-dichroic and dichroic absorbers based on the absence of the second-harmonic term at $4f_M$.

Many practical implementations of PACT prefer handheld transducers [9,10]. We also demonstrated the feasibility of DS-PACT with a handheld linear-array-based PACT system (Fig. 6) to show the effect of fluence modulation. A Nd:YAG laser (532 nm and 50-Hz pulse repetition rate) was used for illumination. The laser beam was coupled into the phantom from the free space and excited the absorbers at an angle of incidence of 30 deg relative to the imaging plane. The polarization of the laser beam was modulated by rotating a half-wave plate at a frequency $f_M = 0.12$ Hz. The generated acoustic waves were detected by a linear array ultrasonic transducer (Visualsonics, Inc., LZ250, 21-MHz center frequency, 78% one-way bandwidth, 256 elements, 23×3 mm^2 array size). The system had a lateral resolution of 190 μm, an axial resolution of 86 μm, and an elevational resolution of 1237 μm.

In our demonstration, a sample was made by embedding a piece of silicone rubber and a linear polarizer in a scattering medium (0.25% Intralipid and 3% agar in distilled water, with a reduced scattering coefficient of ~0.25 mm^{-1}). On the top of these two absorbers, another linear polarizer was embedded in the superficial region [1 mm below the surface, Fig. 6(a)].

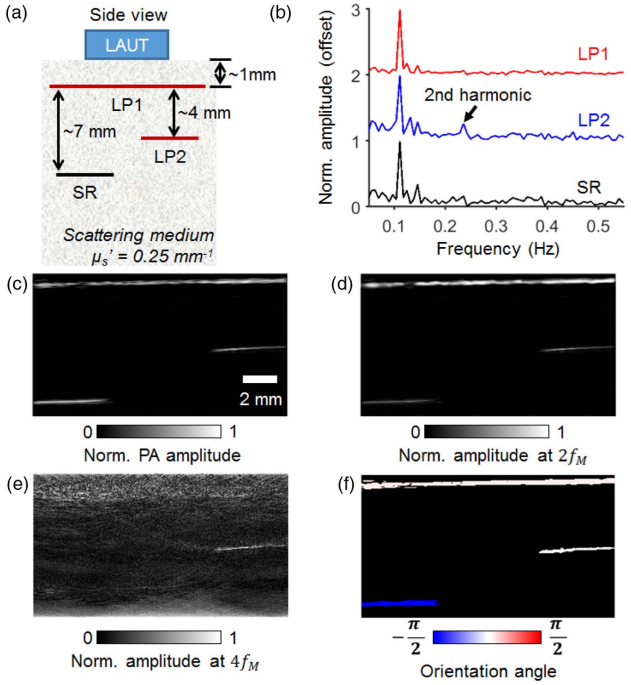

Fig. 6. Demonstration of DS-PACT with a linear array ultrasound transducer (LAUT). (a) Schematic of the phantom. LP, linear polarizer. SR, silicone rubber. (b) Fourier spectra of the linear polarizers and the silicone rubber. Each spectrum is normalized to its first harmonic and offset by 1 with respect to one another. The spectrum of LP2 shows a peak at the second harmonic frequency. (c) Conventional PACT image averaged over 7200 frames. (d) DS-PACT image reconstructed from the amplitude at $2f_M$. (e) DS-PACT image reconstructed from the amplitude at $4f_M$. (f) Orientation angle map.

The Fourier spectrum for each absorber in the sample is shown in Fig. 6(b). As we expected, the Fourier spectrum of the linear polarizer (LP2) in the deep region shows a peak at the second-harmonic frequency. This effect is also confirmed in Fig. 6(e), which is reconstructed from the amplitude at the second-harmonic frequency. Figure 6(f) is a color-coded orientation angle map of both the linear polarizers and the silicone rubber. The spatial distribution of the three absorbers in the sample gave rise to a false orientation angle for the non-dichroic silicone rubber, and the false orientation angle of the silicone rubber is perpendicular to the orientation angle of the top linear polarizer, as our hypothesis. Overall, our method is applicable to a linear-array-based photoacoustic probe, and the false dichroic signal that originated from the fluence modulation can be differentiated by the absence of higher harmonic terms. It has not escaped our attention that other PA imaging modalities can gain a new contrast from the same mechanism as well.

Although the deepest penetration demonstrated in this work was approximately 4.5 l_t', DS-PACT can potentially target deeper as long as a sufficient SNR can be achieved. The ultimate depth is where the light is depolarized due to scattering to the noise level [20,21]. To quantify the depolarizing effect based on pure optical measurements, we measured the speckle contrast after light passed through scattering media with different thicknesses. The speckle contrast is defined as the ratio of the standard deviation to the mean of the speckle intensity. For partially polarized speckles, the speckle contrast C is given by [22]

$$C = \sqrt{\frac{1+P^2}{2}}, \tag{8}$$

where P is the degree of polarization. Therefore, for linearly polarized scattered light ($P = 1$), the speckle contrast is 1, while for completely depolarized scattered light ($P = 0$), the speckle contrast is $1/\sqrt{2}$. Figure 7(a) plots the speckle contrasts after light passes through the scattering media with different thicknesses. The scattered light is gradually depolarized as the scattering medium becomes thicker. Moreover, a small amount of the scattered light is still polarized even at a depth of $6l_t'$, and then the scattered light becomes completely depolarized at a depth of $8l_t'$. Using Eq. (8), Fig. 7(b) plots the degree of polarization as a function of thickness. As shown in the figure, P is around 0.1 even at a depth of $6l_t'$, and reaches almost 0 at a depth of $8l_t'$. The fitted decay constant is $0.4/l_t'$, i.e., 0.1 mm^{-1} given that l_t' is 4 mm,

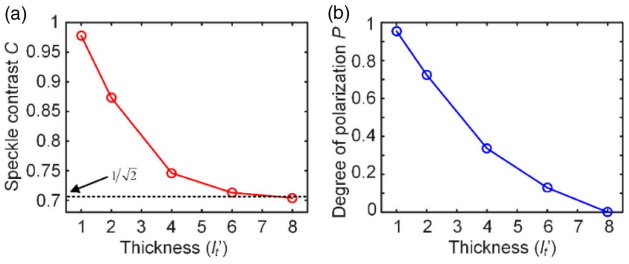

Fig. 7. (a) Speckle contrasts of the scattered light after passing through scattering media with varying thicknesses. The red circles represent the data points, connected by the red solid line. The black dashed line indicates that the scattered light is depolarized to the noise level when the speckle contrast reaches $1/\sqrt{2}$. (b) Degree of polarization as a function of thickness. The blue circles represent the data points, connected by the blue solid line.

which matches well with previous PACT measurements. All these results indicate that the DS-PACT method can image dichroism at a depth of at least $6l_t'$, provided there is a sufficient SNR.

In conclusion, we have developed a new approach to image the dichroism of biological tissues and detect their orientations at a depth much beyond the ballistic regime. Such an approach (DS-PACT) introduces new possibilities for biomedical applications of PACT. For example, the disruption of cell polarity is a hallmark of carcinomas [23], and conventional optical polarization imaging can image this phenomenon [24] with only shallow penetration. DS-PACT may hold a potential for quantifying carcinoma invasion. Further development of our imaging modality could include the use of near-infrared light illumination and a long acquisition sequence to extend the penetration depth. Also, a faster PACT system with single-shot imaging capability and with a higher laser repetition rate will further benefit *in vivo* applications [11].

Funding. National Institutes of Health (NIH) (DP1 EB016986, R01 CA186567, R01 EB016963, U01 NS090579, U01 NS099717); March of Dimes Foundation (3125-17303A).

Acknowledgment. We thank Yan Liu and Liang Gao for helpful discussions and sharing data. We thank Jinyang Liang, Yang Li, Hun He, and Bin Rao for their support in the experiment. We thank Professor James Ballard, Utku Baran, and Sandra Matteucci for proofreading the paper. This project is supported in part by the March of Dimes Prematurity Research Center. K. Maslov has a financial interest in Microphotoacoustics, Inc. L. V. Wang has a financial interest in Microphotoacoustics, Inc., CalPACT, LLC, and Union Photoacoustic Technologies, Ltd., which, however, did not support this work.

See Supplement 1 for supporting content.

†These authors contributed equally to this work.

REFERENCES

1. M. F. Penet, B. Krishnamachary, Z. Chen, J. Jin, and Z. M. Bhujwalla, "Molecular imaging of the tumor microenvironment for precision medicine and theranostics," Adv. Cancer Res. **124**, 235–256 (2014).
2. M. Lakshman and A. Needles, "Screening and quantification of the tumor microenvironment with micro-ultrasound and photoacoustic imaging," Nat. Methods **12**, iii–v (2015).
3. L. V. Wang and S. Hu, "Photoacoustic tomography: in vivo imaging from organelles to organs," Science **335**, 1458–1462 (2012).
4. J. Yao, L. Wang, J. Yang, K. Maslov, T. T. W. Wong, L. Li, C. Huang, J. Zou, and L. V. Wang, "High-speed label-free functional photoacoustic microscopy of mouse brain in action," Nat. Methods **12**, 407–410 (2015).
5. J. Yao, A. A. Kaberniuk, L. Li, D. M. Shcherbakova, R. Zhang, L. Wang, G. Li, V. V. Verkhusha, and L. V. Wang, "Multiscale photoacoustic tomography using reversibly switchable bacterial phytochrome as a near-infrared photochromic probe," Nat. Methods **13**, 67–73 (2016).
6. S. Hu, K. Maslov, P. Yan, J. Lee, and L. V. Wang, "Dichroism optical-resolution photoacoustic microscopy," Proc. SPIE **8223**, 82233T1 (2012).
7. L. Li, J. Yao, and L. V. Wang, *Photoacoustic Tomography Enhanced by Nanoparticles*, Wiley Encyclopedia of Electrical and Electronics Engineering (Wiley, 2016).
8. L. Li, J. Xia, G. Li, A. Garcia-Uribe, Q. Sheng, M. A. Anastasio, and L. V. Wang, "Label-free photoacoustic tomography of whole mouse brain structures ex vivo," Neurophotonics **3**, 0350011 (2016).
9. G. Li, L. Li, L. Zhu, J. Xia, and L. V. Wang, "Multiview Hilbert transformation for full-view photoacoustic computed tomography using a linear array," J. Biomed. Opt. **20**, 066010 (2015).

10. P. Zhang, L. Li, L. Lin, P. Hu, J. Shi, Y. He, L. Zhu, Y. Zhou, and L. V. Wang, "High-resolution deep functional imaging of the whole mouse brain by photoacoustic computed tomography in vivo," J. Biophoton. **11**, c201700024 (2017).
11. L. Li, L. Zhu, C. Ma, L. Lin, J. Yao, L. Wang, K. Maslov, R. Zhang, W. Chen, J. Shi, and L. V. Wang, "Single-impulse panoramic photoacoustic computed tomography of small-animal whole-body dynamics at high spatiotemporal resolution," Nat. Biomed. Eng. **1**, 0071 (2017).
12. J. Xia, M. R. Chatni, K. Maslov, Z. Guo, K. Wang, M. A. Anastasio, and L. V. Wang, "Whole-body ring-shaped confocal photoacoustic computed tomography of small animals in vivo," J. Biomed. Opt. **17**, 0505061 (2012).
13. G. Marriott, S. Mao, T. Sakata, J. Ran, D. K. Jackson, C. Petchprayoon, T. J. Gomez, E. Warp, O. Tulyathan, H. L. Aaron, E. Y. Isacoff, and Y. Yan, "Optical lock-in detection imaging microscopy for contrast-enhanced imaging in living cells," Proc. Natl. Acad. Sci. USA **105**, 17789–17794 (2008).
14. American National Standards Institute, "American National Standard for the safe use of lasers," ANSI Z136.1-2007 (American National Standards Institute, 2000).
15. M. A. Anastasio, J. Zhang, X. Pan, Y. Zou, G. Ku, and L. V. Wang, "Half-time image reconstruction in thermoacoustic tomography," IEEE Trans. Med. Imaging **24**, 199–210 (2005).
16. L. V. Wang and H. Wu, *Biomedical Optics: Principles and Imaging* (Wiley, 2007).
17. M. Born and E. Wolf, *Principles of Optics*, 7th ed. (Cambridge University, 1999).
18. M. Todorović, S. Jiao, L. V. Wang, and G. Stoica, "Determination of local polarization properties of biological samples in the presence of diattenuation by use of Mueller optical coherence tomography," Opt. Lett. **29**, 2402–2404 (2004).
19. R. N. Bracewell, *The Fourier Transform and its Applications*, 3rd ed. (McGraw-Hill, 2000).
20. Y. Shen, Y. Liu, C. Ma, and L. V. Wang, "Focusing light through scattering media by full-polarization digital optical phase conjugation," Opt. Lett. **41**, 1130–1133 (2016).
21. V. Sankaran, J. T. Walsh, and D. J. Maitland, "Comparative study of polarized light propagation in biologic tissues," J. Biomed. Opt. **7**, 300–306 (2002).
22. J. W. Goodman, *Speckle Phenomena in Optics: Theory and Applications* (Roberts and Company, 2007).
23. M. Lee and V. Vasioukhin, "Cell polarity and cancer-cell and tissue polarity as a non-canonical tumor suppressor," J. Cell Sci. **121**, 1141–1150 (2008).
24. V. Backman, R. Gurjar, K. Badizadegan, I. Itzkan, R. R. Dasari, L. T. Perelman, and M. S. Feld, "Polarized light scattering spectroscopy for quantitative measurement of epithelial cellular structures in situ," IEEE J. Sel. Top. Quantum Electron. **5**, 1019–1026 (1999).